npj Climate and Atmospheric Science https://doi.org/10.1038/s41612-026-01423-7

Article in Press

Antarctic ozone as a precursor to winter central asian precipitation beyond ENSO

Received: 14 February 2026

Accepted: 20 April 2026

Cite this article as: Yao, M., Tang, H., Huang, G. *et al.* Antarctic ozone as a precursor to winter central asian precipitation beyond ENSO. *npj Clim Atmos Sci* (2026). https://doi.org/10.1038/s41612-026-01423-7

Mengyuan Yao, Haosu Tang, Gang Huang & James A. Screen

Antarctic Ozone as a Precursor to Winter Central Asian Precipitation Beyond ENSO

Mengyuan Yao[1,2], Haosu Tang[3*], Gang Huang[1,2*], James A. Screen[4]

[1]*Key Laboratory of Earth System Numerical Modeling and Application, Institute of Atmospheric Physics, Chinese Academy of Sciences, Beijing, China*

[2]*University of Chinese Academy of Sciences, Beijing, China*

[3]*School of Geography and Planning, University of Sheffield, Sheffield, UK*

[4]*Department of Mathematics and Statistics, University of Exeter, Exeter, UK*

*Corresponding author: haosu.tang@sheffield.ac.uk and hg@mail.iap.ac.cn

Abstract

Central Asia (CA) experiences large interannual hydroclimate variability that profoundly affects ecosystems, agriculture, and socioeconomic stability. While the El Niño–Southern Oscillation (ENSO) has long been recognized as the leading driver, a significant proportion of observed CA precipitation variability remains unexplained. Here, we reveal that Antarctic ozone variability in October–November serves as a robust and independent precursor to winter CA precipitation (WCAP). Antarctic ozone modulates WCAP through two primary pathways. First, enhanced Antarctic ozone drives a persistent negative phase of the Southern Annular Mode (SAM) that persists into the following winter. The ensuing ozone–SAM coupling shifts two Ferrel cells equatorward and enhances low-level convergence and ascent over CA, thereby increasing WCAP. Second, the negative SAM induces central–eastern South Pacific warming, triggering Rossby wave trains that establish a meridional circulation dipole around CA and strengthen subtropical westerlies, moisture transport, and WCAP. Exposure analyses further indicate that combined ozone–ENSO effects substantially exacerbate precipitation-related socioeconomic risks across CA, adding ~34 billion person-days of population exposure and >34 billion dollar-days of economic exposure by mid-century relative to ENSO alone. Our findings identify Antarctic ozone variability as a critical yet previously underappreciated predictor of CA hydroclimate, revealing subtle interhemispheric connections beyond the traditional ENSO-centric paradigm.

INTRODUCTION

Central Asia (CA), encompassing Kazakhstan, Kyrgyzstan, Uzbekistan, Tajikistan, and Turkmenistan, constitutes the world's largest arid to semi-arid region. Fragile ecosystems and scarce water resources render societies highly vulnerable to hydroclimatic fluctuations [1-3]. Boreal winter Central Asian precipitation (WCAP), especially as snowfall over mountainous terrain, contributes more than half of the annual total [4, 5]. Its spring melt regulates river discharge, irrigation, and ecosystems, thereby shaping agricultural productivity, water availability, and vegetation dynamics in the subsequent warm season [4, 6-8]. Previous studies have shown that a variety of Northern Hemisphere processes, including Indo-Pacific and Atlantic sea surface temperature (SST) anomalies, Arctic sea ice loss, and local land–atmosphere interactions such as snow cover and soil moisture, can significantly influence precipitation over the region [5, 9-13]. However, the role of Southern Hemisphere drivers, especially those originating in the Antarctic, remains insufficiently understood, despite emerging evidence of their potential cross-hemispheric impacts on Northern Hemisphere hydroclimate [14-16]. Hereafter, all seasons mentioned in this study refer to those of the Northern Hemisphere.

Since the late twentieth century, anthropogenic emissions of ozone-depleting substances have produced the Antarctic ozone hole, with seasonal losses of nearly half of the local total-column ozone during boreal autumn. This phenomenon represents one of the clearest examples of human-induced perturbations to the Earth system [17-19]. Meanwhile, interannual variability in Antarctic ozone arises from a combination of dynamical and chemical processes. Variations in planetary wave forcing from the troposphere play a central role by modulating the strength of the polar vortex and meridional ozone transport, while the amplitude and propagation of these waves are further modulated by the quasi-biennial oscillation (QBO) [20, 21]. Beyond its chemical effects, Antarctic ozone variability exerts a broad influence on atmosphere–ocean coupling and climate variability in the Southern Hemisphere from seasonal to decadal timescales. Apart from its radiative forcing on stratospheric temperatures [22, 23], Antarctic ozone variability has emerged as a

potent driver of atmospheric circulation changes, modulating regional temperature and precipitation [18, 24-29]. In addition, the positive phase of the Southern Annular Mode (SAM), the leading mode of extratropical variability in the Southern Hemisphere, can be induced by stratospheric cooling associated with ozone depletion. This strengthens the polar vortex and alters planetary wave propagation, thereby shifting poleward and intensifying the Southern Hemisphere eddy-driven jet [30-32]. Therefore, investigating the potential influence of Antarctic ozone, a key driver of large-scale climate variability, may help bridge current gaps in understanding interhemispheric climate linkages affecting WCAP.

SAM variability is fundamentally linked to interannual fluctuations in stratosphere–troposphere coupling [14, 22, 33, 34], with Antarctic ozone depletion identified as the dominant driver of the observed positive SAM trend in recent decades, exceeding the influence of greenhouse gas forcing [30]. Conversely, SAM in June–August also feeds back on the stratosphere by modulating the strength and position of the polar vortex, whereby a stronger vortex during the positive SAM phase cools the stratosphere, accelerating ozone depletion and deepening the ozone hole in September–November [35]. Additionally, through its imprint on surface winds, Ekman transport, and ocean mixed-layer processes, a positive SAM is conducive to a dipole-like anomalous SST pattern in the southern extratropical ocean, with warming at mid-latitudes and cooling at high latitudes, thereby reshaping atmosphere–ocean feedbacks, including an amplified and poleward-shifted Ferrel cell [18, 36-38]. These pathways establish SAM as a key bridge linking Antarctic ozone to Southern Hemisphere climate variability [26, 27, 29, 38]. Beyond the Southern Hemisphere, SAM anomalies also trigger interhemispheric teleconnections, influencing Northern Hemisphere mid- to high-latitude temperature, East Asian hydroclimate, and the tricellular circulation, with impacts that may persist across seasons [14, 16, 25, 39, 40]. Such evidence indicates that SAM may influence subsequent-season climate anomalies in the Northern Hemisphere [15, 16, 33]. Nevertheless, whether and how the Antarctic ozone–SAM coupling modulates WCAP variability, a key determinant of regional water resources and ecosystem health, has yet to be systematically examined.

This study investigates the interannual variability of WCAP in response to boreal autumn (October–November) Antarctic ozone anomalies during 1979–2023, revealing cross-hemisphere linkages that have so far been underrecognized. While previous work has established the El Niño–Southern Oscillation (ENSO) as the dominant driver of precipitation variability in CA [9, 10, 41, 42], we demonstrate that Antarctic ozone plays a crucial and dynamically independent role as well, acting together with ENSO to shape WCAP variability. Mechanistically, boreal autumn Antarctic ozone anomalies lead SAM variability by approximately one month, and the subsequent ozone–SAM coupling modulates WCAP by altering the global meridional circulation and by interacting with the Walker circulation and triggering eastern Pacific warming, which together shape atmospheric dynamics over CA. These mechanisms are further supported by Coupled Model Intercomparison Project Phase 6 (CMIP6) simulations and atmospheric general circulation model (AGCM) experiments using ECHAM6. Beyond its climatic impacts, Antarctic ozone anomalies superimposed on ENSO events could significantly amplify socioeconomic exposure to hydroclimatic variability in CA, with direct implications for regional risk assessment and adaptation planning.

RESULTS

Lagged WCAP Response to Autumn Antarctic Ozone Variability

We first examine the linear and potentially additive effects of October–November Antarctic ozone on the interannual variability of WCAP. The Antarctic total column ozone index (ATCOI) is defined as the cosine-latitude-weighted mean total column ozone averaged over 60°–90°S, 180°W–180°E, while the Niño3.4 index, representing ENSO intensity, is calculated as the average SST anomaly over 170°–120°W, 5°S–5°N (Methods). To isolate interannual variability, both indices and WCAP are high-pass filtered to remove interdecadal components longer than 11 years (Supplementary Fig. 1). During 1979–2023, interannual WCAP variability exhibits significant correlations with autumn ATCOI and winter Niño3.4, with regional mean correlation coefficients

reaching 0.37 ($p < 0.01$) and 0.52 ($p < 0.01$), respectively. The two indices are statistically independent ($r = -0.07$), indicating that their impacts on WCAP are largely independent and approximately additive (Fig. 1a). In addition, given that the Indian Ocean Dipole (IOD) is a dominant coupled ocean–atmosphere mode on interannual timescales in the tropical Indian Ocean, peaking in boreal autumn and exerting global climate impacts [43, 44], we further examine its relationship with the ATCOI. The autumn ATCOI is found statistically independent of the simultaneous IOD Index ($p > 0.1$), defined as the difference in SST anomalies between the western (50°E–70°E, 10°S–10°N) and southeastern (90°E–110°E, 10°S–0°) Indian Ocean [45]. These results suggest that Antarctic ozone variability can be regarded as a distinct signal, independent of both Pacific and Indian Ocean influences. Spatially, correlation patterns reveal that increased autumn ATCOI is linked to enhanced WCAP east of 60°E, with weaker responses in western CA, whereas winter El Niño induces a more homogeneous wetting across the entire region (Figs. 1b–c). These WCAP patterns linked to ATCOI and ENSO are further validated using independent observational datasets, including Global Precipitation Climatology Centre (GPCC; 1979–2020) and Global Precipitation Climatology Project (GPCP; 1980–2023) (Supplementary Fig. 2).

Additionally, the lead–lag relationship between ATCOI and SAM is examined. The SAM, defined as the normalized zonal mean sea level pressure difference between 40°S and 65°S, exhibits a significant negative correlation ($p < 0.01$) with autumn ATCOI when the latter leads by about one month (Supplementary Fig. 3), indicating that ATCOI and SAM interact during autumn and might jointly shape the subsequent winter circulation anomalies. The negative phase of winter SAM produces a coherent wetting pattern consistent with ATCOI (Fig. 1d and Supplementary Fig. 4), suggesting that autumn ATCOI may modulate WCAP through its interaction with SAM. This wetting linkage between ATCOI and WCAP is further corroborated by the multi-model ensemble mean (MME) of CMIP6 models that realistically simulate WCAP and Antarctic ozone variability (Fig. 1e; Methods).

SAM as a Bridge Linking Antarctic Ozone to WCAP

The above hypothesized bridging role of SAM is supported by moisture budget diagnostics regressed onto autumn ATCOI, the inverted winter SAM and Niño3.4 (Supplementary Fig. 5). Negative normalized SAM anomalies induce a stronger WCAP response (1.34 mm mon^{-1}) than positive normalized ATCOI (1.02 mm mon^{-1}). This difference is consistent with the fact that the winter SAM represents a contemporaneous signal linked to WCAP, whereas autumn ATCOI acts as a precursor with a lagged influence of approximately 1–2 months (Supplementary Fig. 3). Specifically, both negative SAM and positive ATCOI enhance WCAP primarily through dynamic processes driven by anomalous convergence of background moisture, which offsets the drying effect of thermodynamic processes associated with anomalous moisture (Supplementary Fig. 5). Quantitatively, a negative SAM enhances WCAP by up to 139% through dynamical moisture transport, while a positive ATCOI contributes a smaller but still substantial increase of about 119%. In parallel, regression onto normalized Niño3.4 yields a stronger WCAP response of 1.42 mm mon^{-1}, with the dynamical component contributing up to 165%, indicating a dominant contemporaneous influence of ENSO relative to SAM and ATCOI. These findings suggest that winter SAM acts as a critical intermediary linking Antarctic ozone variability to WCAP, with its additional contribution beyond ATCOI likely mediated through interactions with ENSO that modulate interannual WCAP variability.

Given the well-established ENSO–WCAP teleconnection [9, 10, 41, 42], we focus here primarily on ozone-related mechanisms. We first investigate how autumn ATCOI modulates the subsequent SAM, and then how winter ozone–SAM coupling further affects WCAP. Figure 2 illustrates the atmospheric and oceanic responses to enhanced ATCOI. Higher autumn ATCOI favors the negative phase of SAM in both autumn and winter, characterized by a weakened and equatorward-shifted 200-hPa westerly jet at high latitudes (Fig. 2a). This response can be attributed to lower-stratospheric warming at high latitudes, which enhances downward longwave radiation at high latitudes and warms the mid-to-upper troposphere in situ, thereby weakening the climatological

negative meridional temperature gradient between high and mid-latitudes (Fig. 2b). The delayed wintertime response reflects the typical downward propagation of stratospheric signals, which generally take several weeks to months to reach the surface [22, 46].

In addition, the persistent influence of Antarctic ozone induces a quasi-barotropic adjustment of low-level winds (Fig. 2a). Weakened polar westerlies and their equatorward shift linked to the negative phase of SAM strengthen poleward Ekman transport, reducing upwelling and warming high latitudes while enhancing upwelling and cooling at mid-latitudes (Figs. 2c–e). This circulation adjustment promotes a northward shift of the Antarctic Circumpolar Current and the associated meridional overturning circulation, contributing to the formation of a Southern Ocean dipole SST anomaly pattern [18]. These Ekman-driven SST anomalies are further amplified by the wind–evaporation–SST feedback [47, 48]. Reduced high-latitude westerlies suppress surface evaporation, leading to local SST warming, while enhanced mid-latitude westerlies increase evaporation and induce SST cooling. The resulting meridional anomalous SST dipole develops from October–November into December–February and is sustained by surface heat flux anomalies (Supplementary Fig. 6). Specifically, Ekman transport dominates the formation of the anomalous dipole-like SST pattern, while net radiation and turbulent heat flux reinforce the meridional SST gradient. These results indicate that SAM could serve as a useful proxy for understanding how the impacts of autumn ATCOI persist into the following winter.

Potential Mechanisms Linking SAM to WCAP

In this section, we examine the mechanisms through which SAM influences the interannual variability of WCAP via large-scale circulation changes. SAM exerts seasonal impacts on major atmospheric circulation systems, including the Ferrel and Walker cells [14, 28, 34]. On the one hand, SAM and the associated anomalous Southern Ocean dipole SST pattern could directly modulate global meridional circulation along the 45–88°E longitude band that corresponds to CA (Fig. 3a). During the negative SAM phase, the ascent branch of the Southern Hemisphere Ferrel cell

intensifies and shifts equatorward by about 10°, centering around 50°S, while the descent branch also expands equatorward to 10°S, overlapping with the climatological ascent branch of the Hadley cell. This pattern indicates a northward displacement of the Southern Hemisphere Ferrel cell, accompanied by the weakening of the Hadley cell. Meridional atmospheric circulation adjustments in the Southern Hemisphere further influence Northern Hemisphere circulation through the shared ascent branch of the Hadley cell [14, 34, 40]. Consequently, the climatological mid-latitude ascent center in the Northern Hemisphere shifts southward from 60°N to 50°N, enhancing low-level moisture convergence and ascent over CA (red line in Fig. 3a), thereby increasing WCAP.

On the other hand, negative SAM could also modulate tropical convection and weaken the Walker circulation through a Southern Hemisphere–tropical teleconnection pathway excited by SAM-associated South Atlantic–Pacific dipole SST anomaly pattern [49]. Consistent with this mechanism, the zonal atmospheric circulation averaged over 10°S–10°N is regressed onto the inverted SAM index (Fig. 3b). These circulation anomaly changes are accompanied by tropical westerly anomalies in the central-eastern Pacific, which weaken the trade winds and suppress compensatory upwelling, favoring eastern Pacific warming (Fig. 3b). This is supported by a significant negative partial correlation ($r = -0.33$, $p < 0.01$) between SAM (with ENSO signals removed) and the South Pacific Index (SPI), defined as interannual SST anomalies averaged over 130°–70°W, 25°–10°S (magenta box in Fig. 2f). In addition, Walker circulation anomalies associated with winter SPI manifest as a large-scale upper-level divergence–convergence dipole pattern, characterized by upper-level divergence over the central-eastern Pacific and compensating convergence over the Indo-Pacific warm pool (Fig. 3c). As a result, CA lies under the upper divergent flank, where anomalous ascent enhances WCAP, a pattern consistent with divergence fields regressed onto the inverted winter SAM (Figs. 3c, d). These results suggest that SAM variability modulates the Walker circulation and central-eastern Pacific SST anomalies, thereby affecting WCAP through large-scale divergence–convergence dipole anomalies.

Additional evidence for the SAM–SPI linkage comes from regressions of the 200-hPa stream

function onto the inverted winter SAM and the corresponding wave activity flux, which reveal a Rossby wave train originating from the high-latitude South Pacific and propagating into the tropical Pacific, accompanied by low-level tropical westerly anomalies (Figs. 3e–f). Furthermore, the persistent northeastward-propagating, cross-hemispheric Rossby wave train associated with a negative winter SAM extends into the North Atlantic, resulting in upper-level cyclonic anomalies over northern CA and anticyclonic anomalies over southern CA. This meridional dipole anomalous circulation strengthens the 200-hPa subtropical westerly jet and enhances moisture transport from the North Atlantic into CA, ultimately intensifying WCAP (Figs. 3e–f).

The above-mentioned mechanisms are consistently captured by both the CMIP6 MME and targeted numerical experiments (Fig. 4 and Supplementary Fig. 7; Methods). The MME reproduces the ATCOI-related negative phase of SAM and the accompanying dipole-like SST pattern over the Southern Ocean (Supplementary Figs. 7a–b). Meanwhile, the meridional circulation features a weakened Hadley cell and two equatorward-shifted Ferrel cells, with the northern one leading to anomalous moisture convergence and ascent in CA (Supplementary Fig. 7c). Upper-level divergence and ascent over CA are further enhanced through the large-scale divergence–convergence dipole spanning the Indian and Pacific Oceans, favoring increased WCAP (Supplementary Fig. 7d).

To further corroborate the modulation of WCAP by autumn ATCOI, a sensitivity experiment is performed using the ECHAM6 model. The imposed SST forcing over the extratropical Southern Ocean (75°S–30°S) is based on the autumn SST pattern regressed onto the ATCOI, with the amplitude ranging from −0.27 to 0.17 K, whose influence on SST variability is supported by a Granger causality test at the 90% confidence level (Fig. 4a). This forcing reproduces the homogeneous wetting across CA (Fig. 4b). Dynamically, the imposed SST anomalies induce an expansion of the descending branch of Southern Hemisphere Ferrel cell over 50°S–15°S, accompanied by a southward displacement of the Northern Hemisphere Ferrel circulation. The latter enhances moisture convergence and anomalous ascent over CA, particularly over its northern

part, despite enhanced ascent over the equator compared with observations (Fig. 4c). In addition, the ATCOI–SAM coupling generates pronounced upper-level divergence over the eastern Pacific and the western to northern sectors of the Atlantic–Eurasian region, while compensating convergence occupies the western Indian Ocean and the Maritime Continent (Fig. 4d). CA lies along the divergent flank of this large-scale divergence–convergence dipole and is therefore dominated by upper-level divergence anomalies, which favor enhanced ascent and low-level moisture convergence, ultimately intensifying WCAP (Fig. 4d). Although the resulting circulation patterns exhibit slight differences from observations, these discrepancies do not alter the overall conclusion that the meridional pathway triggered by the imposed SST anomalies exerts a robust influence on the WCAP.

Combined Effects of SAM and ENSO on WCAP Variability

Previous studies have shown that atmospheric teleconnections originating from the South Pacific intensify when SAM and ENSO are in opposite phases, affecting climate variability over North America and Eurasia [50]. However, simple correlation analyses often inadequately capture SAM-modulated changes in ENSO teleconnections due to their sensitivity to outliers [48, 50]. To address this, we conduct further composite analyses comparing individual SAM events with coupled out-of-phase winter SAM–ENSO events. Specifically, using ±0.75 as the standard deviation threshold, out-of-phase events are defined as cases in which both indices exceed the threshold but with opposite signs, whereas individual events are cases where only one index exceeds the threshold (Supplementary Table 1). The reference climatology is defined as the composite mean of events in which both indices fall within ±0.5 standard deviations.

The results indicate that negative SAM coupled with El Niño produces more homogeneous and intensified wetting, with a spatially averaged WCAP anomaly of 5.90 mm mon^{-1}, especially in southeastern CA. This response is substantially stronger than that during individual negative SAM events, which yield a weaker wetting anomaly of 2.23 mm mon^{-1}. The additional increase

in WCAP during the combined events, relative to individual negative SAM events, is associated with a strengthened Pacific–North America (PNA) wave train and more pronounced upper-level divergence–convergence anomalies over the Pacific (first and second rows in Fig. 5). In contrast, positive SAM coupled with La Niña results in drier conditions of −1.50 mm mon^{-1} in CA, compared with −0.20 mm mon^{-1} during individual positive SAM events. During individual positive SAM events, CA is located within the upper-level convergence over the Indo-Pacific warm pool, dominated by a 200-hPa anticyclonic anomaly that promotes subsidence and suppresses WCAP (third row in Fig. 5). Simultaneously, a cyclonic circulation over South Asia transports warm and moisture-laden air from the Indian Ocean into southern CA, partly offsetting the drying. When positive SAM co-occurs with La Niña, however, CA is located near the margin of the warm pool divergence zone, where prevailing subsidence anomalies further suppress WCAP (fourth row in Fig. 5). The resulting decrease in WCAP is partially compensated by cyclonic anomalies over central CA, which form part of the South Pacific Rossby wave train and thereby enhancing WCAP in the region (fourth row in Fig. 5). Nevertheless, the strong anticyclone over South Asia blocks moisture transport from the Indian Ocean, intensifying drought in southern CA. These results remain generally robust to the use of an alternative ±0.5 standard deviation threshold (Supplementary Fig. 8). Notably, a consistent enhancement of WCAP is also observed in composites based on autumn ATCOI and the subsequent winter mature ENSO phase, where in-phase coupling leads to intensified WCAP anomalies (Supplementary Fig. 9).

Predictability and Socioeconomic Exposure of WCAP

The autumn ATCOI–ENSO-based composite analysis, examined under both 0.75 and 0.5 standard deviation thresholds, shows high consistency with winter SAM–ENSO composite responses (Supplementary Figs. 10–11), providing a robust physical basis for WCAP predictability. Given the cross-seasonal effects of ATCOI and ENSO on WCAP and their approximately linear additivity, both predictors are taken as their October–November mean values. Using linear

regressions over the training period (1979–2010), the prediction equation is established as WCAP = −0.06 + 0.94×ATCOI + 1.40×Niño3.4. Leave-one-out cross-validation yields a temporal correlation coefficient of 0.55 ($p < 0.01$) and a root mean square error (RMSE) of 4.53 mm mon^{-1} in the training period. Forecast skill remains robust in the independent prediction period (2011–2023), with $r = 0.58$ and RMSE = 5.67 mm mon^{-1} (Fig. 6a). To further assess robustness, ATCOI is replaced by alternative physically interpretable indices, namely winter (December–February) or early-winter (December–January) SAM combined with Niño3.4, as well as a cross-seasonal combination of autumn (October–November) ATCOI and winter Niño3.4 at their respective peak phases. All predictor sets yield high predictive skill, with correlation coefficients exceeding 0.58 and RMSEs below 5.28 mm mon^{-1} (Supplementary Fig. 12).

Building on this predictive model, we assess the socioeconomic exposure associated with WCAP variability. Figures 6b–c present the spatial distributions of averaged population (POP) and Gross Domestic Product (GDP) across CA in the 2010s, indicating that socioeconomic assets are predominantly concentrated along oasis regions of southern and northern CA. These spatial patterns reflect underlying geographic and developmental factors, instead of direct exposure. We therefore quantify area-averaged exposure, focusing on the contributions of different climate drivers to CA-averaged POP and GDP, rather than spatial variability. Specifically, regional exposure is estimated by multiplying one standard deviation of reconstructed WCAP anomalies induced by ATCOI, Niño3.4, and their combined effect during 1979–2023 with projected POP and GDP (Figs. 6d–e). This approach assumes that the empirical predictor–WCAP relationships remain valid in the near future, enabling the estimation of additional exposure attributable to ATCOI from the excess of combined effects over ENSO alone (Methods).

Under the business-as-usual Shared Socioeconomic Pathways 2 (SSP2) scenario, ATCOI and ENSO individually contribute more than 210 billion person-days of POP exposure during 2020–2060, while their combined effect adds 31–34 billion person-days relative to Niño3.4 alone across the first half of the 21st century. Under the fossil-fuel-driven SSP5 scenario, POP exposure is

slightly lower than in SSP2 but remains broadly stable. In contrast, GDP exposure exhibits a pronounced decadal increase. Under SSP2, WCAP-driven GDP exposure attributable to ATCOI, ENSO, and their combined effect increases by 155, 182, and 205 billion dollar-days (2010 Purchasing Power Parity) from 2020 to 2060, respectively. These corresponding values surge to 283, 333, and 375 billion dollar-days under the SSP5 scenario. Importantly, the additional GDP exposure contributed by ATCOI relative to ENSO alone increases from 11 to 34 billion dollar-days under SSP2, while from 11 to 53 billion dollar-days under SSP5 during 2020–2060. These results indicate that the ozone-driven component further amplifies hydroclimatic exposure beyond the ENSO-related baseline. Consequently, Antarctic ozone-induced WCAP variability may intensify climate risks in the rapidly developing CA region, and proactive adaptation and water resource management would therefore be beneficial.

DISCUSSION

This study establishes the stratosphere, particularly autumn Antarctic ozone variability, as an underappreciated source of seasonal predictability for CA hydroclimate, independent of the dominant influence of ENSO. In this world's largest arid and semi-arid region, winter precipitation accounts for more than half of the annual total and is therefore critical for regional hydrology, agriculture, and ecosystems [4, 5]. Our results demonstrate that enhanced autumn Antarctic ozone induces a negative phase of SAM in the following winter, providing a key dynamical bridge linking cross-hemispheric ozone variability to CA hydroclimate. The schematic in Fig. 7 summarizes the key mechanisms identified in this study.

Mechanistically, SAM modulates WCAP via two distinct pathways. First, the equatorward expansion of the Southern Hemisphere Ferrel cell and associated southward displacement of the Northern Hemisphere Ferrel circulation favor anomalous ascent and low-level moisture convergence over CA. Second, SAM weakens the Walker circulation via a Southern Hemisphere–tropical teleconnection pathway, thereby favoring El Niño–like warming in the central-eastern

Pacific. The resulting large-scale divergence–convergence dipole reflecting tropical convection anomalies places CA along the upper-level divergent flank, favoring ascent and WCAP. When SAM and ENSO act out of phase, their combined effects further amplify WCAP anomalies beyond those induced by individual SAM events.

Building on these mechanisms, we develop a physically based linear prediction model for WCAP using autumn ATCOI and Niño3.4. The model exhibits robust predictive skill, with a correlation coefficient of 0.58 and an RMSE of 5.67 mm mon^{-1} during the independent prediction period (2011–2023), and comparable performance is achieved using alternative physically interpretable predictors, including winter SAM and cross-seasonal combinations of ATCOI and ENSO. Moreover, the relevant socioeconomic implications are substantial, with ATCOI-related variability projected to increase exposure by more than 34 billion person-days of POP and 34 billion dollar-days of GDP by the 2060s under the SSP2 scenario, and could reach 53 billion dollar-days under the high-emission SSP5 scenario. These results highlight the socioeconomic significance of Antarctic ozone–related WCAP variability and its joint predictive potential with ENSO to improve climate risk prediction in CA.

Importantly, the exploration of SST forcing also provides a practical framework to isolate and quantify the contributions of individual ocean basins. To further disentangle these basin-specific effects, we perform three additional sensitivity experiments in which the SST dipole anomalies are imposed separately over the Pacific, Indian, and Atlantic sectors of the Southern Ocean, as indicated by the boxes in Fig. 4a. The results show that SST dipole forcing in all three basins generally favors increased precipitation over CA, except for southern CA in the Indian Ocean experiment (Supplementary Fig. 13). Across all basin-specific experiments, the descending branch of the Southern Hemisphere Ferrel cell expands equatorward, while the Northern Hemisphere Ferrel circulation shifts southward, jointly enhancing low-level moisture convergence and anomalous ascent over CA, thereby increasing WCAP. Notably, the equatorial responses differ among basins. The Indian and Atlantic Ocean experiments exhibit enhanced equatorial ascent,

whereas the Pacific experiment features weaker equatorial ascent, in closer agreement with observations (Fig. 3a and Supplementary Figs. 13b, d, f). These contrasts suggest basin-dependent modulation of the ATCOI–WCAP teleconnection, and the relative dominance and potential interactions among the Southern Ocean dipole forcings across different basins warrant further investigation.

In addition to precipitation, interannual variability of winter near-surface air temperature (T2m) in CA is assessed as well. Its variability is significantly correlated with the tropical signal (Niño3.4; $p < 0.1$), whereas its relationships with autumn ATCOI and winter SAM are weak and statistically insignificant (Supplementary Fig. 14). Further, several uncertainties remain to be elucidated in the future, including the asymmetric responses arising from SAM–ENSO interactions [50, 51] and different ENSO phases [52, 53]. Additionally, previous findings indicated that Atlantic Multidecadal Variability (AMV) shapes WCAP at interdecadal timescales through Rossby wave train propagation [54]. Although Antarctic ozone recovery and the associated positive SAM shift may modulate WCAP, their impacts on longer timescales are largely obscured by low-frequency climate modes, resulting in only weak correlations at the interdecadal timescale ($r = 0.28$ and -0.33 during 1979–2023). As the Antarctic ozone hole continues to recover under international ozone-depleting substance intervention, its evolving impacts on SAM, interhemispheric teleconnections, and the CA hydroclimate warrant sustained monitoring. Integrating both interannual and decadal predictors, such as ATCOI, ENSO, and AMV, into climate risk assessments promises to improve early-warning capacity and inform water resource management, thereby strengthening climate resilience across this highly vulnerable region.

METHODS

Data

Three monthly precipitation datasets are used to ensure the robustness of the results. These include the Climatic Research Unit (CRU) high-resolution gridded dataset (version 4.04), GPCC monthly product (version 2022), and GPCP monthly analysis product (version 2.3) [55, 56]. Monthly T2m data are sourced from CRU as well. SST fields are obtained from the Hadley Centre Sea Ice and SST dataset (HadISST) [57]. Additionally, atmospheric circulation variables, surface radiative fluxes, and total column ozone are derived from the fifth-generation European Centre for Medium-Range Weather Forecasts atmospheric reanalysis (ERA5) [58]. Meanwhile, population and economic projections at national and provincial scales under the Shared Socioeconomic Pathways (SSPs) are incorporated, covering the period 2010–2100 [59].

Outputs from historical experiments of nine CMIP6 climate models (see details in Supplementary Table 2) are also analyzed. These represent the only models currently providing publicly available outputs for both total-column ozone and precipitation. These simulations, covering the period 1850–2014, reproduce past climate conditions under combined natural and anthropogenic forcings, thus offering an extensive ensemble to examine the mechanisms driving historical WCAP variability. The model evaluation, based on a Taylor diagram analysis, indicates that all nine models reasonably capture the climatological features of WCAP and Antarctic total-column ozone (Supplementary Fig. 15). Moreover, all models except GISS-E2-2-G realistically reproduce the Antarctic ozone variability (Supplementary Fig. 16). To avoid sampling bias, GISS-E2-2-G is retained in the ensemble, and sensitivity tests confirm that its exclusion does not affect the overall conclusions. For consistency, all model datasets are bilinearly interpolated onto a common 1° × 1° grid before analysis. Model agreement is assessed using a significance criterion requiring at least 70% consistency in the sign of the multi-model response.

In the present study, winter is defined as December of the preceding year to February of the current year. Unless otherwise specified, all seasons refer to those of the Northern Hemisphere.

The research period spans 1979–2023, with 1979–2008 used as the climatological baseline. Analyses using the full 1979–2023 period as the baseline yield consistent results, indicating that our findings are robust to the choice of baseline period. In addition, the starting year of 1979 is selected because the availability of comprehensive satellite observations in the Southern Hemisphere from this time onward ensures robust and consistent records of circulation, ozone, and related climate variables.

Numerical simulations

To examine the modulation of WCAP by the ATCOI-induced dipole-like SST anomaly pattern, numerical experiments are conducted using the AGCM ECHAM6, which constitutes the atmospheric component of the fully coupled MPI Earth System Model (MPI-ESM) [60]. The model is configured at a Gaussian T63 horizontal resolution (96 × 192 grid points) with 47 vertical levels extending up to 0.01-hPa, representing a high-top configuration suitable for resolving stratospheric dynamics. The control simulation (CTL) is driven by global climatological SST and sea ice concentration (SIC) fields that include a realistic seasonal cycle. To isolate the atmospheric response to the ATCOI-related Southern Ocean SST dipole, four sensitivity experiments are conducted by prescribing autumn SST anomalies derived from the Theil–Sen linear regression against the ATCOI. In the first sensitivity experiment, SST anomalies are imposed over the extratropical Southern Ocean (75°S–30°S). In the remaining three experiments, the SST forcing is applied separately to individual ocean basins, including the Pacific Ocean sector (160°E–70°W, 75°S–30°S; black box in Fig. 4a), the Indian Ocean sector (10°E–160°E, 75°S–30°S; magenta box), and the Atlantic Ocean sector (10°E–70°W, 75°S–30°S; green box). Outside these regions, SST and SIC fields are identical to those in the CTL simulation. All experiments are run for a 31-year period, with the last 25 years used for analysis.

ATCOI, SAM and Niño3.4 index

The Antarctic total-column ozone index (ATCOI) is defined as the cosine-latitude-weighted

mean total-column ozone from ERA5 reanalysis over October–November, averaged across 60°–90°S and 180°W–180°E for 1979–2023. October–November is selected as it corresponds to the peak of Antarctic ozone depletion, during which its variability exerts the strongest impact on atmospheric circulation. To validate the ERA5 dataset, we also use ground-based measurements from Halley station (75°S, 25°W), where observations extend from late August to mid-April. Although limited to 1979–2021 due to missing records, the Halley series shows a strong correlation with ERA5-derived ATCOI ($p < 0.001$), confirming its consistency. The reliability of ERA5-derived total-column ozone and the ATCOI definition has also been validated in previous studies.

The Southern Annular Mode (SAM) index is calculated following Marshall (2003), as the normalized zonal mean sea level pressure difference between 40°S and 65°S. Positive SAM phases correspond to enhanced westerlies at 50°–70°S and weakened westerlies at 30°–50°S. The Niño3.4 index is defined as the mean SST anomaly over 170°–120°W, 5°S–5°N, averaged for December–February. All indices are high-pass filtered to exclude interdecadal variations longer than 11 years, allowing robust assessment of the interannual variability (Supplementary Fig. 1).

Moisture budget analysis

To elucidate the physical processes underlying WCAP variability, we conduct a moisture budget analysis based on the vertically integrated moisture equation [61]:

$$P' = \underbrace{-\langle\overline{\overrightarrow{V_3}}\nabla q'\rangle}_{Therm}\underbrace{-\langle\overrightarrow{V_3}'\nabla\bar{q}\rangle}_{Dyn} + E' + \delta' \quad (1)$$

where P', E', and δ' denote anomalies of precipitation, evaporation, and the residual term, respectively. $\overrightarrow{V_3}$ and q indicate the three-dimensional wind and specific humidity fields, respectively. $\langle\,\rangle$ represents the mass integral from the surface to 100-hPa. The prime indicates anomalies relative to the climatological mean, which is denoted by the overbar. The first term on the right-hand side represents the moisture-driven thermodynamic component, associated with anomalous moisture transport by the mean circulation, while the second term represents the circulation-driven dynamic component, linked to anomalous advection of background moisture.

Surface heat flux

To investigate the ocean–atmosphere coupling processes, we analyze surface heat fluxes derived from reanalysis products. Net surface radiation fluxes are computed as the sum of net shortwave and net longwave fluxes, while surface turbulent fluxes are obtained as the sum of latent and sensible heat fluxes. In addition, the Ekman heat flux is calculated as following:

$$Q_{Ek} = \rho C_p (U_{Ek} \cdot \nabla SST) \tag{2}$$

where ρ is seawater density, C_p is the specific heat capacity, ∇SST denotes the SST gradient, and U_{Ek} is the Ekman transport. The Ekman transport is further defined as:

$$U_{Ek} = \frac{1}{\rho f}(-\tau_y, \tau_x) \tag{3}$$

where τ_x and τ_y represent the zonal and meridional surface wind stresses, respectively, and f is the Coriolis parameter.

Wave-activity fluxes

The horizontal wave-activity fluxes are defined as [62]:

$$W = \frac{1}{2|\vec{V}|}\begin{Bmatrix} \bar{U}(\psi_x'^2 - \psi'\psi'_{xx}) + \bar{V}(\psi'_x\psi'_y - \psi'\psi'_{xy}) \\ \bar{U}(\psi'_x\psi'_y - \psi'\psi'_{xy}) + \bar{V}(\psi'^2_y - \psi'\psi'_{yy}) \end{Bmatrix} \tag{4}$$

where $\vec{V}$ represents the horizontal wind velocity vector, U and V denote the zonal and meridional wind velocity, respectively. ψ symbolizes the stream function. The primes and overbars signify anomalies and the climatological mean-state, respectively.

Leave-one-out cross-validation approach

To assess the robustness and predictive skill of the reconstruction model, we employ a leave-one-out cross-validation approach. During the training period (1979–2010), one year is iteratively excluded from the sample, and the model is recalibrated using the remaining years. The excluded year is then reconstructed and compared with observations. Repeating this process for each year

in the training period yields a cross-validated estimate of model performance that is less sensitive to overfitting and provides a more realistic measure of out-of-sample skill. For the independent prediction period (2011–2023), predictions are generated using the regression model calibrated solely on the 1979–2010 training period. This separation between training and independent prediction periods ensures that the evaluation reflects genuine predictive capacity rather than statistical artifacts of model fitting. Such cross-validation has been successfully applied in previous physics-based predictions [63-65].

Exposure assessment

To quantify the socioeconomic impacts associated with WCAP variability, we estimate POP and GDP exposure attributable to ENSO, Antarctic total column ozone, and their combined effect. Exposure is defined as follows:

$$\begin{aligned} \text{Exposure}_i &= W_i \cdot S_{\text{CA}} \\ &= |\,\beta_i\,| \cdot \sigma_i \cdot S_{\text{CA}} \end{aligned} \tag{5}$$

where W_i denotes the weight of driver i in WCAP variability, and S_{CA} represents the CA-averaged POP or GDP. For individual drivers (ATCOI and Niño3.4), W_i is quantified as the product of the absolute regression coefficient ($|\,\beta_i\,|$) derived from the prediction model and the corresponding interannual standard deviation (σ_i) over 1979–2023. For the combined contribution, W_i is estimated from the regression-based WCAP reconstruction, defined as the product of the standard deviation of the reconstructed WCAP (σ_i) and its correlation with observations ($|\,\beta_i\,|$), thereby accounting for both variability amplitude and explained variance. Moreover, the additional contribution attributable to ATCOI is defined as the residual beyond ENSO, which is the difference between the combined and ENSO-related components. Future exposure is calculated using SSP-based projections, while holding the historical sensitivities (i.e., W_i) fixed.

Granger causality analysis

Granger causality analysis is employed to assess directional predictive relationships between

October–November ATCOI and SST anomalies over the Southern Hemisphere mid- to high latitudes (Fig. 4a). Unlike correlation analysis, this approach tests whether the inclusion of past information from a predictor improves the prediction of a target variable, thereby providing a statistical measure of causality in terms of predictability [66].

At each grid point, a bivariate Granger causality test is performed between the predictor time series X (ATCOI) and the response time series Y (SST). The test is based on a vector autoregressive framework, in which the current value of Y is regressed on its own lagged values and those of X. If the inclusion of lagged values of X significantly improves the prediction of Y, X is said to Granger-cause Y.

ACKNOWLEDGMENT

This work was supported by the National Natural Science Foundation of China (42530606, 42261144687) and the National Key R&D Program of China (Project No. 2025YFF0812000).

AUTHOR CONTRIBUTIONS

M.Y. and H.T. were responsible for conceptualization. M.Y. conducted the investigation, curated and analyzed the data, and prepared the original draft, with subsequent review and editing. H.T. contributed to methodology development and formal analysis, and also participated in manuscript review and editing. G.H. supervised the project, secured funding, and managed project administration. J.A.S. and G.H. provided critical input during review and editing. All authors have read and approved the final version of the manuscript.

DATA AVAILABILITY

All the data that support the findings in the present study are available for open acc ess. The monthly precipitation datasets of CRU, GPCC, and GPCP are accessed from htt ps://crudata.uea.ac.uk/cru/data/hrg/cru_ts_4.07, https://opendata.dwd.de/climate_environment/G PCC, and https://www.ncei.noaa.gov/data/global-precipitation-climatology-project-gpcp-month ly/access/, respectively. The monthly HadISST dataset and the global atmospheric circulati on dataset are obtained from https://www.metoffice.gov.uk/hadobs/hadisst and https://cds.cli mate.copernicus.eu/datasets/, respectively. POP and GDP datasets are downloaded from htt ps://www.scidb.cn/en/detail?dataSetId=73c1ddbd79e54638bd0ca2a6bd48e3ff#, respectively. C MIP6 model simulations are derived from https://aims2.llnl.gov/search/cmip6/.

CODE AVAILABILITY

All the codes for analyses and diagnostics are available from the corresponding authors upon reasonable request.

COMPETING INTERESTS

The authors declare no competing financial or non-financial interests.

REFERENCES

1. Jiang, P., Yuan, Y. & Li, Q. Advanced precipitation enhances vegetation primary productivity in Central Asia. *Ecological Indicators.* **166**, 112276 (2024).

2. Su, Y. et al. Gaining water bodies by climate change benefits water crisis mitigation in central Asia. *Science Bulletin.* **70**, 2322-2329 (2025).

3. Schär, C., Vasilina, L., Pertziger, F. & Dirren, S. Seasonal Runoff Forecasting Using Precipitation from Meteorological Data Assimilation Systems. *J Hydrometeorol.* **5**, 959-973 (2004).

4. Apel, H. et al. Statistical forecast of seasonal discharge in Central Asia using observational records: development of a generic linear modelling tool for operational water resource management. *Hydrol Earth Syst Sci.* **22**, 2225-2254 (2018).

5. Gerlitz, L. et al. Variability of the Cold Season Climate in Central Asia. Part I: Weather Types and Their Tropical and Extratropical Drivers. *J Clim.* **31**, 7185-7207 (2018).

6. Qin, Y. et al. Agricultural risks from changing snowmelt. *Nat Clim Change.* **10**, 459-465 (2020).

7. Barlow, M. A. & Tippett, M. K. Variability and Predictability of Central Asia River Flows: Antecedent Winter Precipitation and Large-Scale Teleconnections. *J Hydrometeorol.* **9**, 1334-1349 (2007).

8. Huang, F., Feng, T., Guo, Z. & Li, L. Impact of Winter Snowfall on Vegetation Greenness in Central Asia. *Remote Sens.* **13**, 4205 (2021).

9. Chen, Z., Wu, R., Zhao, Y. & Wang, Z. Different Responses of Central Asian Precipitation to Strong and Weak El Niño Events. *J Clim.* **35**, 1497-1514 (2022).

10. Yao, M., Tang, H., Huang, G. & Wu, R. Interdecadal shifts of ENSO influences on Spring Central Asian precipitation. *npj Clim Atmos Sci.* **7**, 194 (2024).

11. Chen, X., Jia, X., Wu, R. & Qian, Q. Interannual Variation and Prediction of Wintertime Precipitation in Central Asia. *J Clim.* **35**, 4771–4789 (2022).

12. Ying, K., Jiang, D., Zheng, X. & Zhong, L. Potential predictability of seasonal precipitation over Central Asia and its primary sources. *Clim Dyn.* **63**, 168 (2025).

13. Wenli, L. I. U., Zhang, C., Yong, Z. & Yuxin, L. Influences of soil moisture anomalies in May on June precipitation in Central Asia. *Arid Land Geography.* **47**, 38-47 (2024).

14. Liu, T., Li, J. & Zheng, F. Influence of the Boreal Autumn Southern Annular Mode on Winter Precipitation over Land in the Northern Hemisphere. *J Clim.* **28**, 8825-8839 (2015).

15. Liu, T. et al. Influence of the May Southern annular mode on the South China Sea summer monsoon. *Clim Dyn.* **51**, 4095-4107 (2018).

16. Zheng, F., Li, J., Wang, L., Xie, F. & Li, X. Cross-Seasonal Influence of the December–February Southern Hemisphere Annular Mode on March–May Meridional Circulation and Precipitation. *J Clim.* **28**, 6859-6881 (2015).

17. Solomon, S. Stratospheric ozone depletion: A review of concepts and history. *Rev*

Geophys. **37**, 275-316 (1999).

18. Thompson, D. W. J. et al. Signatures of the Antarctic ozone hole in Southern Hemisphere surface climate change. *Nat Geosci.* **4**, 741-749 (2011).

19. Randel, W. J. & Wu, F. A stratospheric ozone profile data set for 1979–2005: Variability, trends, and comparisons with column ozone data. *J Geophys Res.* **112**, D06313 (2007).

20. Shindell, D. T., Rind, D. & Balachandran, N. Interannual Variability of the Antarctic Ozone Hole in a GCM. Part II: A Comparison of Unforced and QBO-Induced Variability. *J Atmos Sci.* **56**, 1873-1884 (1999).

21. Shindell, D. T., Wong, S. & Rind, D. Interannual Variability of the Antarctic Ozone Hole in a GCM. Part I: The Influence of Tropospheric Wave Variability. *J Atmos Sci.* **54**, 2308-2319 (1997).

22. Grise, K. M., Thompson, D. W. J. & Forster, P. M. On the Role of Radiative Processes in Stratosphere–Troposphere Coupling. *J Clim.* **22**, 4154-4161 (2009).

23. Randel, W. J. & Wu, F. Cooling of the Arctic and Antarctic Polar Stratospheres due to Ozone Depletion. *J Clim.* **12**, 1467-1479 (1999).

24. Xie, F. et al. Improved Global Surface Temperature Simulation using Stratospheric Ozone Forcing with More Accurate Variability. *Sci Rep.* **8**, 14474 (2018).

25. Zhu, L. & Wu, Z. Climatic influence of the Antarctic ozone hole on the East Asian winter precipitation. *npj Clim Atmos Sci.* **7**, 184 (2024).

26. Damiani, A. et al. Connection between Antarctic Ozone and Climate: Interannual Precipitation Changes in the Southern Hemisphere. *Atmosphere.* **11**, 579 (2020).

27. Gonzalez, P. L. M., Polvani, L. M., Seager, R. & Correa, G. J. P. Stratospheric ozone depletion: A key driver of recent precipitation trends in south eastern South America. *Climate Dynamics.* **42**, 1775–1792 (2014).

28. Hu, Y. & Fu, Q. Observed poleward expansion of the Hadley circulation since 1979. *Atmos Chem Phys.* **7**, 5229-5236 (2007).

29. Son, S.-W., Purich, A., Hendon, H. H., Kim, B.-M. & Polvani, L. Improved seasonal forecast using ozone hole variability? *Geophys Res Lett.* **40**, 6231-6235 (2013).

30. Polvani, L. M., Waugh, D. W., Correa, G. J. P. & Son, S.-W. Stratospheric Ozone Depletion: The Main Driver of Twentieth-Century Atmospheric Circulation Changes in the Southern Hemisphere. *J Clim.* **24**, 795-812 (2011).

31. Son, S.-W. The impact of stratospheric ozone recovery on the Southern Hemisphere westerly jet. *Science.* **320**, 1486-1489 (2008).

32. Thompson, D. W. J. & Solomon, S. Interpretation of recent Southern Hemisphere climate change. *Science.* **296**, 895-899 (2002).

33. Zheng, F., Li, J. & Liu, T. Some advances in studies of the climatic impacts of the Southern Hemisphere annular mode. *Journal of Meteorological Research.* **28**, 820-835 (2014).

34. Viswambharan, N. & Mohanakumar, K. Changes in the Walker and Hadley circulations associated with the Southern Annular Mode. *Theor Appl Climatol.* **117**, 535-547 (2014).

35. Lee, J. N. & Wu, D. L. Dynamic Impact of the Southern Annular Mode on the Antarctic Ozone Hole Area. **17**, 835 (2025).

36. Li, F., Newman, P. A. & Waugh, D. W. Impacts of Stratospheric Ozone Recovery on Southern Ocean Temperature and Heat Budget. *Geophys Res Lett.* **50**, e2023GL103951 (2023).

37. Jucker, M. & Goyal, R. Ozone-Forced Southern Annular Mode During Antarctic Stratospheric Warming Events. *Geophys Res Lett.* **49**, e2021GL095270 (2022).

38. Zheng, F., Li, J., Feng, J., Li, Y. & Li, Y. Relative Importance of the Austral Summer and Autumn SAM in Modulating Southern Hemisphere Extratropical Autumn SST. *J Clim.* **28**, 8003-8020 (2015).

39. Lin, H., Yu, B. & Hall, N. M. J. Link of the Warm Arctic Cold Eurasian pattern to the Southern Annular Mode variability. *npj Clim Atmos Sci.* **8**, 225 (2025).

40. Liu, T., Li, J., Feng, J., Wang, X. & Li, Y. Cross-Seasonal Relationship between the Boreal Autumn SAM and Winter Precipitation in the Northern Hemisphere in CMIP5. *J Clim.* **29**, 6617-6636 (2016).

41. Mariotti & Annarita. How ENSO impacts precipitation in southwest central Asia. *Geophys Res Lett.* **34**, 370-381 (2007).

42. Chen, X., Wang, S., Hu, Z., Zhou, Q. & Hu, Q. Spatiotemporal characteristics of seasonal precipitation and their relationships with ENSO in Central Asia during 1901–2013. *J Geogr Sci.* **28**, 1341-1368 (2018).

43. Saji, N. H., Goswami, B. N., Vinayachandran, P. N. & Yamagata, T. A dipole mode in the tropical Indian Ocean. *Nature.* **401**, 360-363 (1999).

44. Saji, N. H. & Yamagata, T. Possible impacts of Indian Ocean Dipole mode events on global climate. *Clim Res.* **25**, 151-169 (2003).

45. Yang, Y. et al. Seasonality and Predictability of the Indian Ocean Dipole Mode: ENSO Forcing and Internal Variability. *J Clim.* **28**, 8021-8036 (2015).

46. Hall, R. J., Mitchell, D. M., Seviour, W. J. M. & Wright, C. J. Tracking the Stratosphere-to-Surface Impact of Sudden Stratospheric Warmings. *J Geophys Res Atmos.* **126**, e2020JD033881 (2021).

47. Zheng, F., Li, J., Kucharski, F., Ding, R. & Liu, T. Dominant SST Mode in the Southern Hemisphere Extratropics and Its Influence on Atmospheric Circulation. *Adv Atmos Sci.* **35**, 881-895 (2018).

48. Zheng, F., Li, J. & Ding, R. Influence of the Preceding Austral Summer Southern Hemisphere Annular Mode on the Amplitude of ENSO Decay. *Adv Atmos Sci.* **34**, 1358–1379 (2017).

49. Wu, Z., Dou, J. & Lin, H. Potential influence of the November–December Southern Hemisphere annular mode on the East Asian winter precipitation: a new mechanism. *Clim Dyn.* **44**, 1215-1226 (2015).

50. Fogt, R. L., Bromwich, D. H. & Hines, K. M. Understanding the SAM influence on the South Pacific ENSO teleconnection. *Clim Dyn.* **36**, 1555-1576 (2011).

51. Fogt, R. L., Jones, J. M. & Renwick, J. Seasonal Zonal Asymmetries in the Southern Annular Mode and Their Impact on Regional Temperature Anomalies. *J Clim.* **25**, 6253-6270 (2012).

52. Zhang, P. et al. Why East Asian monsoon anomalies are more robust in post El Niño than in post La Niña summers. *Nat Commun.* **15**, 7401 (2024).

53. Beniche, M. et al. A distinct and reproducible teleconnection pattern over North America during extreme El Niño events. *Sci Rep.* **14**, 2457 (2024).

54. Yao, M., Tang, H. & Huang, G. Roles of External Forcing and Internal Variability in Winter Precipitation Changes Over Central Asia. *Earths Future.* **13**, e2025EF006064 (2025).

55. Adler, R. F. et al. The Global Precipitation Climatology Project (GPCP) monthly analysis (new version 2.3) and a review of 2017 global precipitation. *Atmosphere.* **9**, 138 (2018).

56. Adler, R. F. et al. The version-2 global precipitation climatology project (GPCP) monthly precipitation analysis (1979–present). *J Hydrometeorol.* **4**, 1147-1167 (2003).

57. Rayner, N. et al. Global analyses of sea surface temperature, sea ice, and night marine air temperature since the late nineteenth century. *J Geophys Res Atmos.* **108**, 4407 (2003).

58. Hersbach, H. et al. The ERA5 global reanalysis. *Q J R Meteorol Soc.* **146**, 1999–2049 (2020).

59. Tong, J. et al. National and provincial population and economy projection databases under Shared Socioeconomic Pathways(SSP1-5)_v2. (2024).

60. Giorgetta, M. A. et al. Climate and carbon cycle changes from 1850 to 2100 in MPI‐ESM simulations for the Coupled Model Intercomparison Project phase 5. *Journal of Advances in Modeling Earth Systems.* **5**, 572-597 (2013).

61. Yao, M., Tang, H. & Huang, G. Inter-Model Uncertainty in Projecting Precipitation Changes Over Central Asia Under Global Warming. *Geophys Res Lett.* **51**, e2024GL111989 (2024).

62. Takaya, K. & Nakamura, H. A Formulation of a Phase-Independent Wave-Activity Flux for Stationary and Migratory Quasigeostrophic Eddies on a Zonally Varying Basic Flow. *J Atmos Sci.* **58**, 608–627 (2001).

63. Zhou, Z., Li, J., Chen, H. & Zhu, Z. Seasonal Prediction of Extreme High-Temperature Days in Southwestern China Based on the Physical Precursors. *Adv Atmos Sci.* **40**, 1212-1224 (2023).

64. Yao, M., Li, J., Zheng, C., Yao, M. & Zhu, Z. How predictable is the anomaly pattern of summer extreme high-temperature days over Central Asia? *Clim Dyn.* **62**, 7651–7664 (2024).

65. Li, J., Zheng, C., Yang, Y., Lu, R. & Zhu, Z. Predictability of spatial distribution of pre-summer extreme precipitation days over southern China revealed by the physical-based empirical model. *Clim Dyn.* **61**, 2299–2316 (2023).

66. Sun, K. et al. Spatiotemporal correlations and driving factors of multiple drought in Central Asia. *Atmos Res.* **324**, 108199 (2025).

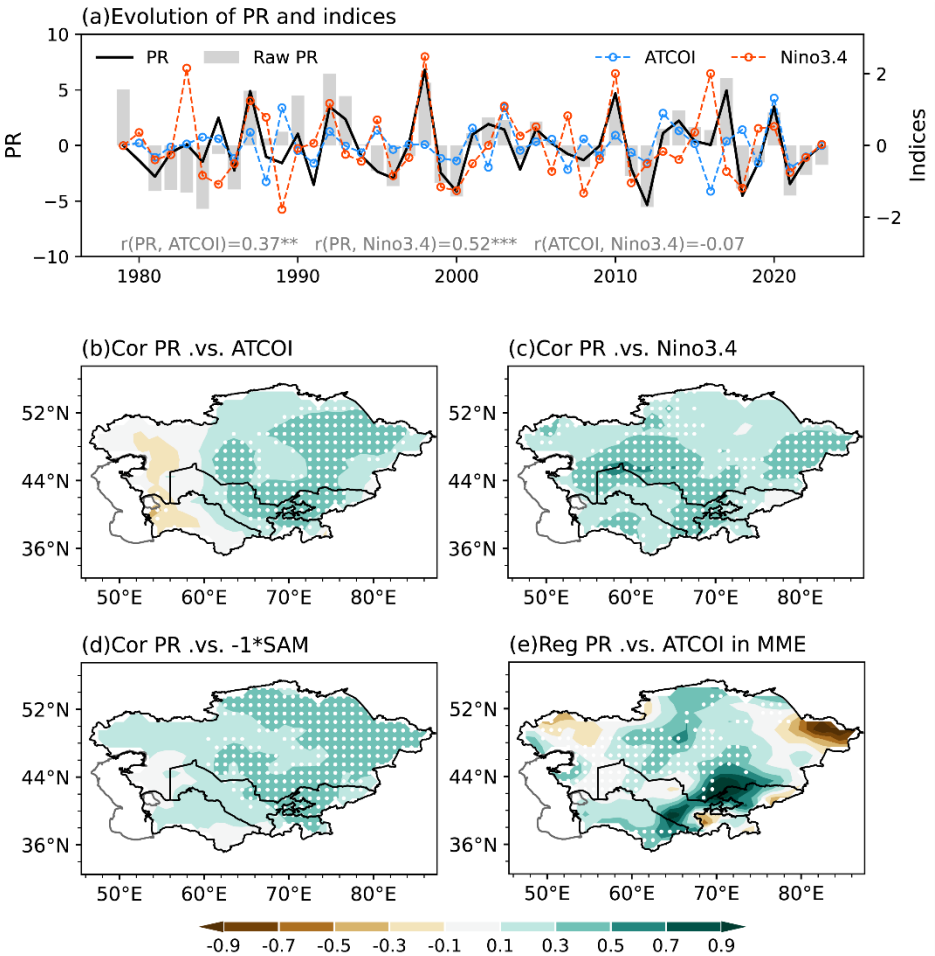

Fig. 1 | Interannual variability of WCAP and its large-scale climate drivers. (a) Time series of interannual WCAP anomalies (PR; black line; units: mm mon^{-1}), ATCOI in preceding October–November (blue line; units: 10^{-3} kg m $^{-2}$) and winter Niño3.4 index (red line; units: °C) from 1979 to 2023. Gray bars represent raw PR. Numbers below denote their correlation coefficients, with three asterisks indicating significance at the 99% confidence level. (b–d) Spatial distributions of correlation coefficients of PR with autumn ATCOI, winter Niño3.4, and inverted winter SAM, respectively. White dots indicate regions with significant correlation coefficients at the 90% confidence level. (e) Same as (b), but for CMIP6 model simulations in 1979–2014. White dots indicate regions with at least 70% consistency in CMIP6 models.

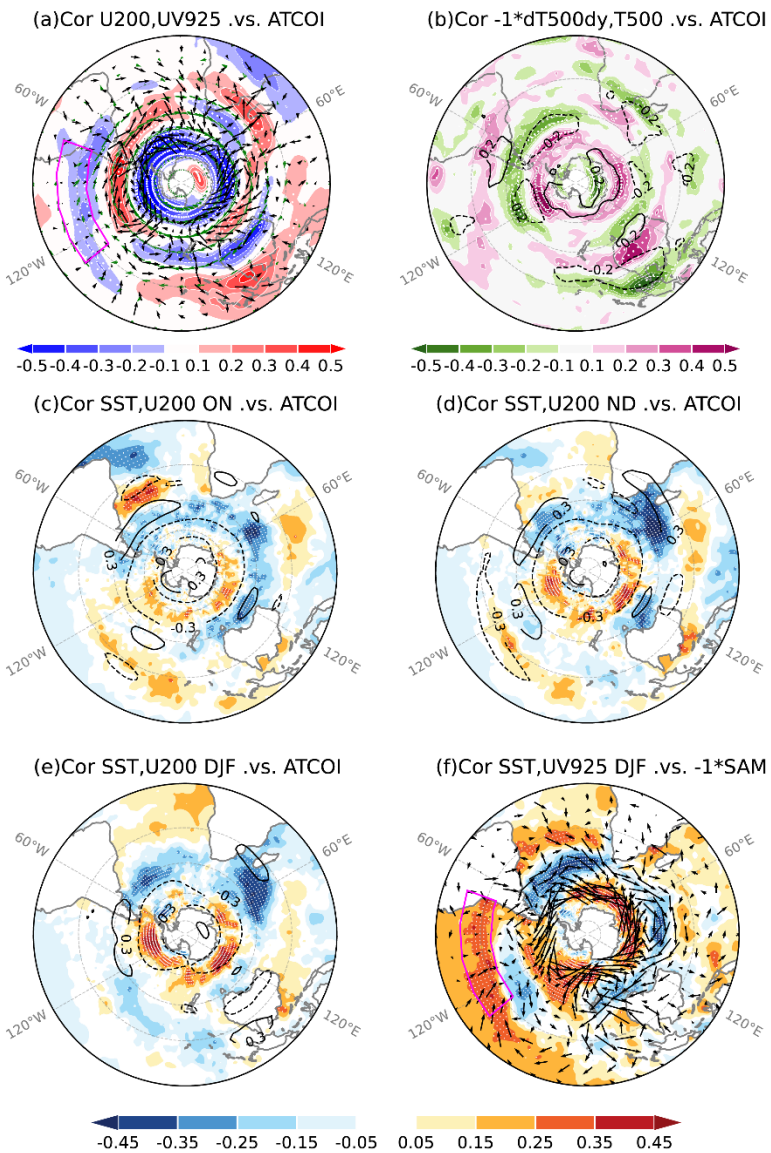

Fig. 2 | Atmospheric circulation responses to autumn ATCOI and associated SST anomalies. (a) Correlation map of ATCOI with winter 200-hPa zonal wind (shading) and 925-hPa wind vectors (black vectors). Green vectors denote climatological 200-hPa winds. (b) Correlation map of ATCOI with winter 500-hPa temperature (contours) and its meridional gradient ($-\frac{\partial T}{\partial y}$, positive northward; shading). Solid (dashed) contours denote positive (negative) correlations. (c–e) Correlation maps of ATCOI with SST (shading) and 200-hPa zonal wind (contours) in simultaneous October–November, November–December, and the following December–February, respectively. (f) Correlation map of inverted winter SAM with SST (shading) and 925-hPa wind vectors (black vectors) in the simultaneous December–February period. The magenta boxes in (a, f) denote the SPI region (130°–70°W, 25°–10°S). White dots indicate regions with significant correlation coefficients at the 90% confidence level.

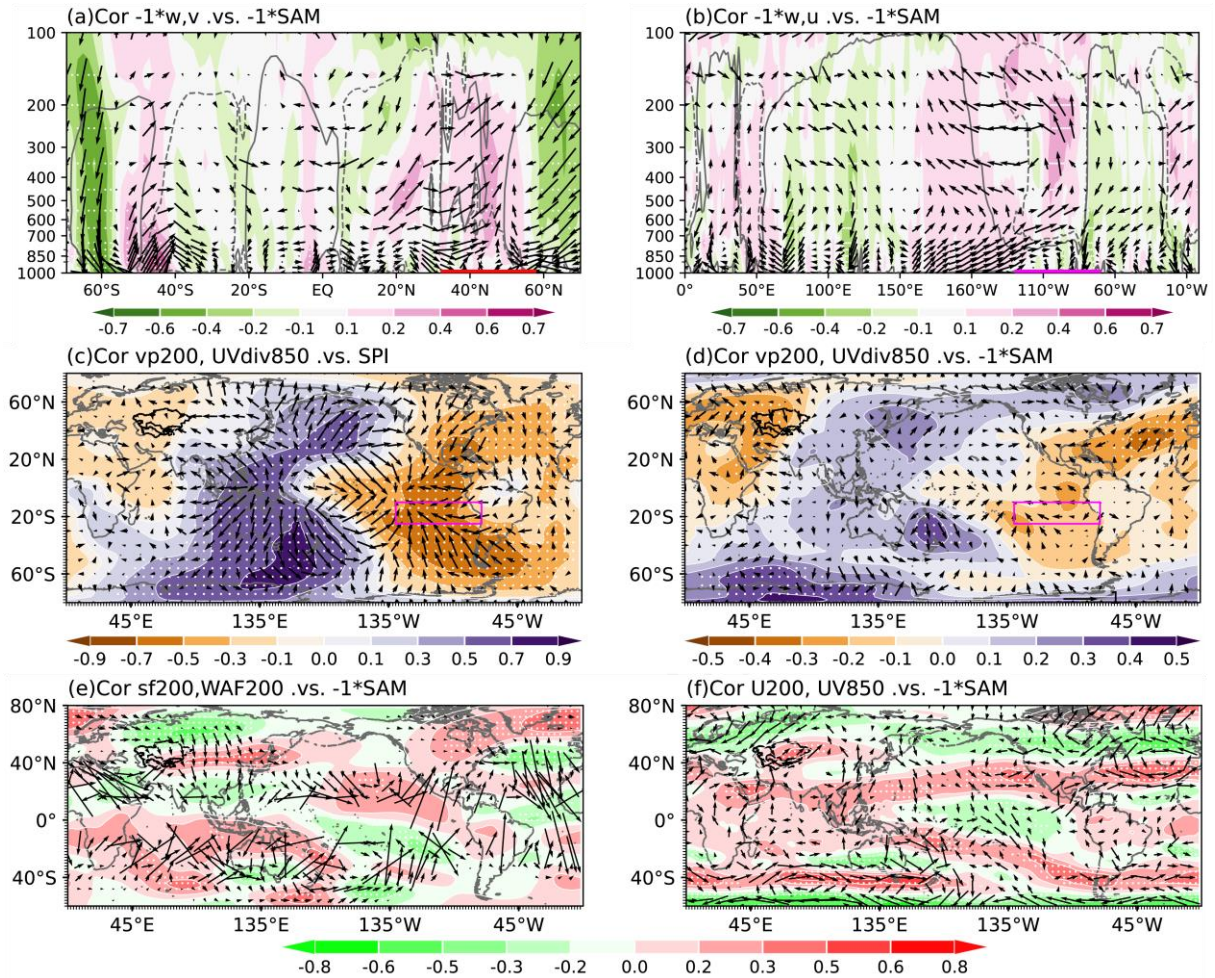

Fig. 3 | Winter atmospheric circulation responses to inverted winter SAM and winter SPI. (a) Latitude–height distribution of correlation coefficients between inverted SAM and the meridional circulation averaged over 45°–88°E (vectors) and inverted vertical velocity (shading; positive values denote ascending). The red horizontal line on the x-axis marks CA at 32°–58°N. (b) Longitude–height distribution of correlation coefficients between inverted SAM and the zonal circulation averaged over 10°S–10°N (vectors) and inverted vertical velocity (shading; positive values denote ascending). The magenta horizontal line on the x-axis marks the SPI region at 130°–70°W. Contours in (a–b) denote the climatology of inverted vertical velocity of $\pm 3\times10^{-3}$ Pa s^{-1}. (c–d) Correlation maps of SPI and inverted SAM with 200-hPa velocity potential (shading) and 850-hPa divergent wind (vectors), respectively. (e) Correlation map of inverted SAM with 200-hPa stream function (shading) and the corresponding 200-hPa wave activity flux (vectors; only values exceeding 0.1 are shown). (f) Correlation map of inverted SAM with 200-hPa zonal wind (shading) and 850-hPa wind (vectors; only values exceeding 0.1 are shown). Dots indicate regions with significant correlation coefficients at the 90% confidence level.

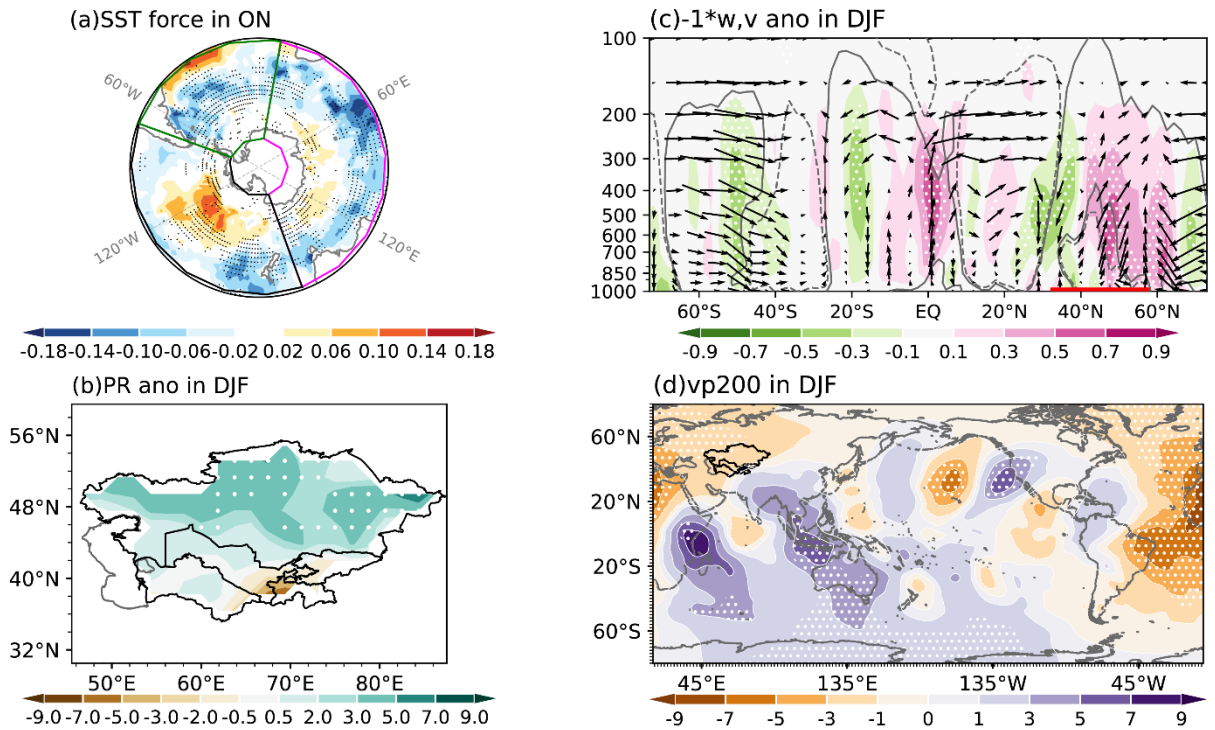

Fig. 4 | Winter atmospheric responses to the Southern Ocean SST forcing associated with autumn ATCOI. (a) Prescribed autumn SST forcing (unit: K) over the Southern Ocean (75°S–30°S). The black, magenta, and green boxes indicate the Pacific, Indian, and Atlantic sectors of the extratropical Southern Ocean (75°S–30°S), respectively. (b) WCAP response (unit: mm month^{-1}). Black dots indicate regions where the Granger causality test is significant at the 90% confidence level. (c) Meridional circulation response (vectors) of meridional wind (unit: m s^{-1}) and inverted vertical velocity (unit: 10^{-2} Pa s^{-1}; shading; positive values denote ascending) anomalies averaged over 45°–88°E. The red horizontal line on the x-axis marks CA at 32°–58°N. Contours denote the climatology of inverted vertical velocity of $\pm 3\times10^{-3}$ Pa s^{-1}. (d) 200-hPa velocity potential anomalies (unit: 10^5 m^2 s^{-1}; shading). White dots denote regions with significant differences between the forced response and climatology at a 90% confidence level.

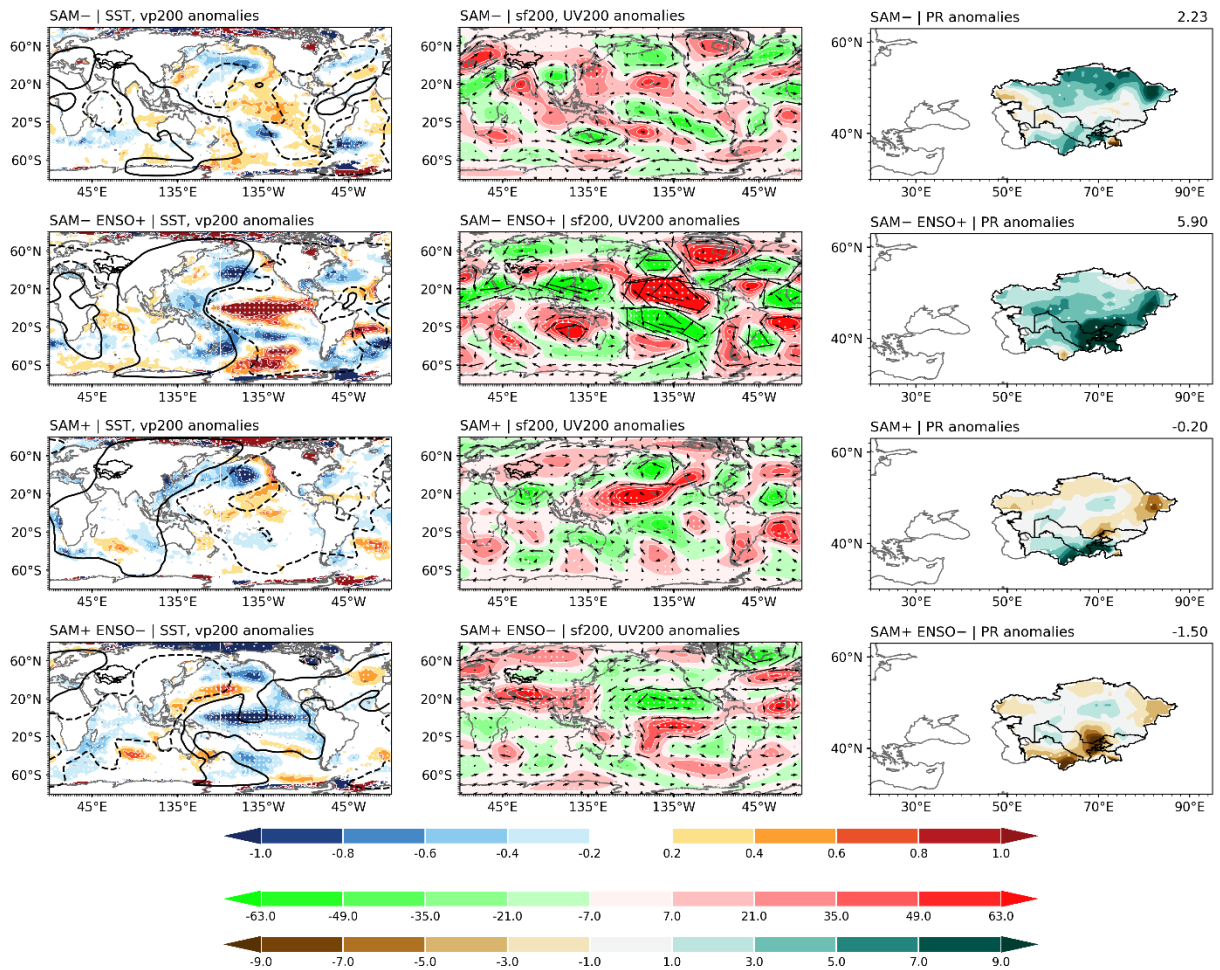

Fig. 5 | Winter atmospheric circulation responses to the out-of-phase relationship between winter SAM and ENSO. The phases of SAM and ENSO are determined by a threshold of 0.75, as summarized in Table S1. The first column shows composites of SST (shading; units: °C) and 200-hPa velocity potential (contours; values of $\pm 5 \times 10^5$ m^2 s^{-1}) anomalies. The second and third columns display composites of 200-hPa stream function (shading; units: 10^6 m^2 s^{-1}), horizontal wind (shading; units: m s^{-1}) and PR (shading; units: mm mon^{-1}) anomalies, respectively. White dots indicate regions with significant correlation coefficients at the 90% confidence level.

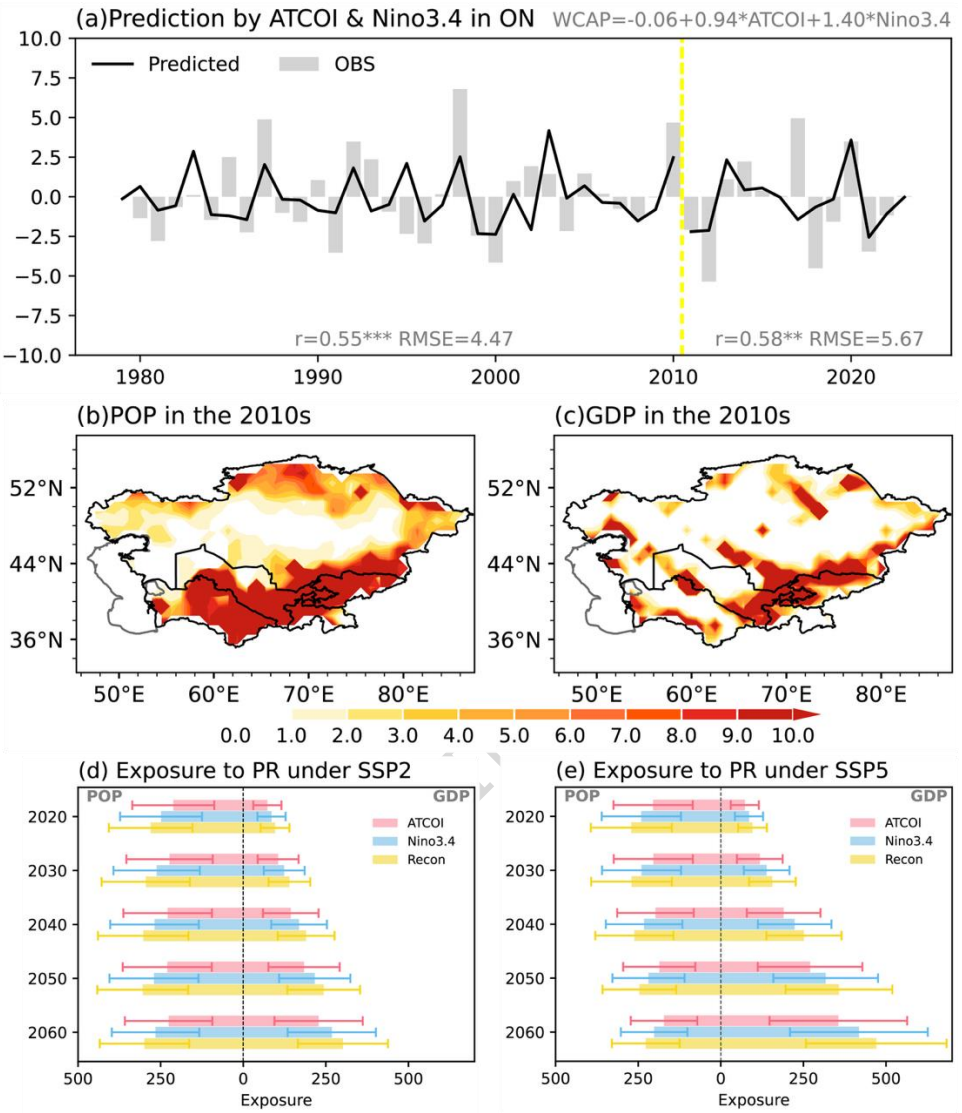

Fig. 6 | Reconstruction and socioeconomic impacts of WCAP. (a) Observed (OBS; gray bars; unit: mm mon^{-1}) and reconstructed WCAP anomalies (black line; unit: mm mon^{-1}) based on normalized preceding October–November ATCOI and Niño3.4 index. Prediction equations are shown in the upper-right corner, and prediction skills during the training and independent prediction periods are indicated at the bottom-left and bottom-right, respectively. One, two, and three asterisks denote significance at the 90%, 95%, and 99% confidence levels, respectively. The yellow dashed line marks the separation between the training and independent prediction periods, located between 2010 and 2011. (b–c) POP (unit: 100 million persons) and GDP (unit: billion dollars, 2010 price) over CA during the 2010s. (d–e) Exposure to internal WCAP variability induced by one standard deviation of ATCOI (red bar), Niño3.4 (blue bar), and the reconstruction (yellow bar) under SSP2 and SSP5 scenarios, respectively. POP exposure is expressed in billion person-days, and GDP exposure is in billion dollar-days (2010 price, Purchasing Power Parity). Error bars denote the 95% confidence interval.

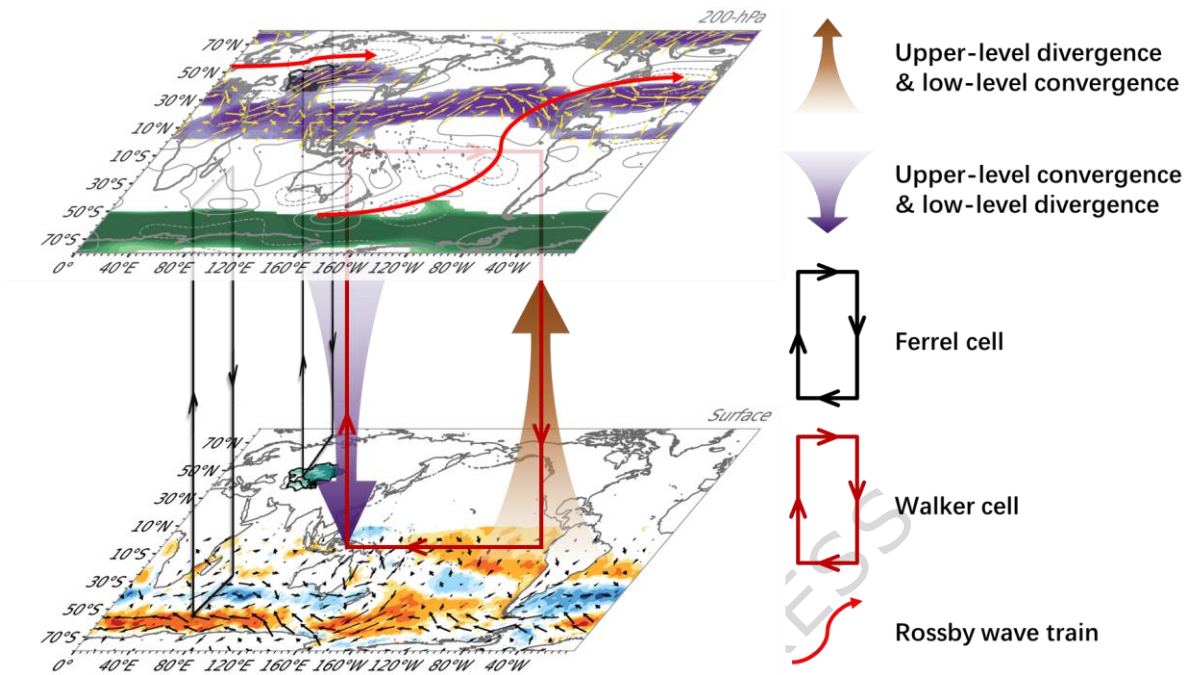

Fig. 7 | Schematic diagram illustrating the mechanisms of enhanced autumn Antarctic ozone to interannual WCAP variability. At the surface, blue and orange shadings denote negative and positive winter SST anomalies, respectively, while green shading indicates increased WCAP. Black vectors represent 925-hPa wind anomalies. At 200-hPa, purple and green shadings indicate strengthened and weakened zonal winds, respectively, with yellow arrows marking the horizontal wind anomalies associated with strengthened westerlies. Gray solid (dashed) contours represent positive (negative) stream function anomalies to depict the wave train excited by enhanced autumn Antarctic ozone. The red curves illustrate the propagation of Rossby wave trains. Symbols connecting the two atmospheric layers denote vertical coupling. Brown vector indicates upper-level divergence with lower-level convergence, whereas purple denotes the opposite configuration. Black and red circulations depict the Ferrel and Walker cells, respectively.